Three-Dimensional Cell Printed Lock-Key Structure for Oral Soft and Hard Tissue Regeneration

Shihan Zhang, PhD,[1,2,*] Qing Li, PhD,[1–3,*] Peng Liu, PhD,[1,2] Chunping Lin, PhD,[1]
Zhihui Tang, PhD,[1,i] and Hom-Lay Wang, DDS, PhD[4]

Alveolar ridge absorbs rapidly following tooth extraction. To promote implant rehabilitation, an adequate bone and soft tissue volume are required. Three-dimensional (3D) cell printing technique provides the advantages of precise spatial distribution and personalization. In this study, 3D cell printing was used to establish a soft-hard construct that is composed of alginate/gelatin (AG)/gingival fibroblast cells (GFs) and alginate/gelatin/nano-hydroxyapatite (AGH)/bone marrow-derived mesenchymal stem cells (BMSCs). Physicochemical results showed that nano-hydroxyapatite (nHA) added in the bioink maintained its crystalline phase. In addition, an increase of viscosity, the improvement of compressive modulus ($p < 0.01$), and slow degradation rate ($p < 0.01$) were found after adding nHA. SEM showed cell stretched and attached well on the surface of the 3D printed construct. At day 7 after printing, the viability of GFs in AG was $94.80\% \pm 1.14\%$, while BMSC viability in AGH was $86.59\% \pm 0.75\%$. Polymerase chain reaction results indicated that the expression levels of *ALP*, *RUNX-2*, and *OCN* in BMSCs were higher in AGH than AG bioink ($p < 0.01$). After 8-week implantation into the dorsum of 6- to 8-week-old male athymic and inbred (BALB/c) nude mice, the cellular printed construct displayed a more integrated structure and better healing of subcutaneous tissue compared with the acellular printed construct. In conclusion, this 3D cell printed soft-hard construct exhibits favorable biocompatibility and has potential for alveolar ridge preservation.

Keywords: 3D cell printing, gingival fibroblast cells, bone marrow-derived mesenchymal stem cells, lock-key structure, soft and hard tissue regeneration

Impact Statement

Alveolar ridge resorption after tooth extraction has posed great difficulty in the subsequent restorative procedure. Clinically, to preserve the dimension of alveolar ridge, covering soft tissue healing and underlying bone formation is necessary after tooth extraction. Three-dimensional (3D) cell printing, which can distribute different biomaterials and cells with spatial control, provides a novel approach to develop a customized plug to put in the fresh socket to minimize bone resorption and improve gingiva growth. In this study, an integrated and heterogeneous soft-hard construct with lock-key structure was successfully developed using 3D cell printing. The physicochemical and biological properties were tested *in vitro* and *in vivo*. This 3D cell printed soft-hard construct will be a customized plug in alveolar ridge preservation in the future.

Introduction

ALVEOLAR PROCESS IS the supporting tissue of the teeth, which is composed of the gingiva and underlying alveolar bone. In general, 6 months after tooth extraction, a 29–63% and 11–22% bone resorption in the width and height were expected,[1–3] which make it difficult for implant placement especially in the esthetic zone. Even though various alveolar ridge preservation techniques were proposed to overcome this problem with different outcomes, there is a demand to enhance covering soft tissue healing and bone regeneration. Gingiva healing can minimize

---

[1]Second Clinical Division, Peking University School and Hospital of Stomatology, Beijing, China.
[2]National Engineering Laboratory for Digital and Material Technology of Stomatology, Beijing, China.
[3]Center of Digital Dentistry, Peking University School and Hospital of Stomatology, Beijing, China.
[4]Department of Periodontics and Oral Medicine, University of Michigan School of Dentistry, Ann Arbor, Michigan, USA.
*These authors contributed equally to this work.
[i]ORCID ID (https://orcid.org/0000-0002-0522-7306).

surgical complications (e.g., gingiva shrinkage and dehiscence) and provide an ideal, functional, and esthetic foundation for prosthetic rehabilitation.[4,5] Three-dimensional (3D) bioprinting is a newly proposed approach that may provide an integrated soft-hard construct to improve the clinical outcomes.

A conventional 3D bioprinting process, consisting of manual cell seeding over the scaffold, exhibits some limitations, including a nonhomogenous cell distribution and poor controllability of architecture.[6,7] The improved 3D cell printing technique can establish a cell-laden construct using various bioinks.[8,9] This 3D structure has been shown to facilitate cell proliferation and differentiation *in situ*.[10] By adopting bottom-up strategy, bioinks deposit cells layer-by-layer according to their desired characterization, which contributes to the controllable spatial distribution of different biomaterials and cells.[11] These unique properties play a critical role for cell organization that is needed to generate a heterogeneous and integrated soft-hard construct. Furthermore, customized geometry and porosity of the construct could be established during the printing process.[12]

The combination of alginate/gelatin (AG) in the construct exhibited improvement of reepithelialization and collagen synthesis after skin injury.[13] Although AG serves as a versatile bioink in 3D bioprinting, its physiological properties and biological activity are inadequate to support osteogenesis in hard tissue engineering.[14,15] Nano-hydroxyapatite (nHA) is a suitable substitute for inorganic components in natural bone mineral.[16,17] Due to superior osteoconductive property, nHA has become a popular nanomaterial, to be added into bioink to enhance osteogenesis especially in bone tissue engineering.[18–20] Therefore, in this study, AG/gingival fibroblast cells (GFs) and alginate/gelatin/nano-hydroxyapatite (AGH)/bone marrow-derived mesenchymal stem cells (BMSCs) were used, respectively, to establish a soft-hard construct with the lock-key structure to improve the regeneration in alveolar process.

Early attempts of using 3D cell printing have focused on establishing a heterogeneous construct in articular cartilage and skin regeneration, but none for extensive clinical practice.[21–24] The tooth extraction socket appears to be a good model for testing this newly developed soft-hard cell printed construct since it provides a stable environment for soft and hard tissue regeneration.[25] Hence, the aim of this study was to create a 3D cell printed soft-hard construct using two types of bioinks for the socket healing and to evaluate its biocompatibility.

Materials and Methods

Cell and bioink preparation

Human BMSCs (ScienCell Research Laboratory, Carlsbad, CA) and human GF lines (Stomatology School and Hospital of Peking University) between 2 and 5 passages were used in the experiments. According to the report from the supplier, *CD90*, one of the MSC surface-specific antigens, is positive on the surface of BMSCs. Vimentin is positive but *CD31* is negative on the surface of GFs. The cells were cultured in proliferation medium (PM), composed of Dulbecco's modified Eagle's medium (DMEM) supplemented with 10% fetal bovine serum and 1% antibiotics, and stored at 37°C in an incubator. Osteogenic medium (OM) for the differentiation of BMSCs was freshly prepared before its addition to the cell culture, which contained 100 nM dexamethasone, 50 mM l-ascorbic acid, and 10 mM β-glycerophosphate.

Sodium alginate powders (Cat no. 180947; Sigma-Aldrich) with the viscosity of 15–25 cP (1% in H_2O), Gelatin from porcine skin (Cat no. 180947, Type A, 300 bloom; Sigma-Aldrich), and nHA (average size 100 nm, MW:502.31) (YuanyeBio-Technology, Shanghai, China) were sterilized by ultraviolet (UV) irradiation for 60 min and then dissolved into phosphate-buffered saline (PBS) at 37°C and incubated for 1 day to form bioink. The 3D extrusion-based bioprinter (Medprin, China) was used for bioprinting the soft-hard construct (Fig. 1). Three types of bioinks were loaded into 1 mL syringes (as shown in Fig. 2b) to measure the printability of the 2 wt% alginate −8 wt% gelatin with different nHA contents (AG, AG +3% nHA, AG +5% nHA).
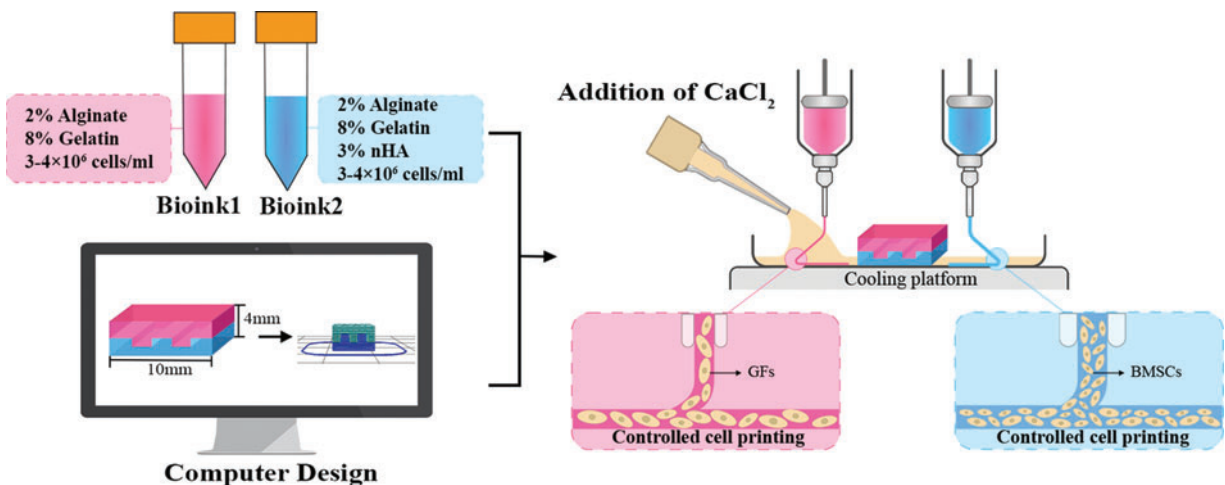

FIG. 1. Schematic illustration of the cell printing procedure to establish the soft-hard construct with lock-key structure using the extrusion-based 3D bioprinter. 3D, three-dimensional; BMSCs, bone marrow-derived mesenchymal stem cells; GFs, gingival fibroblast cells; nHA, nano-hydroxyapatite. Color images are available online.
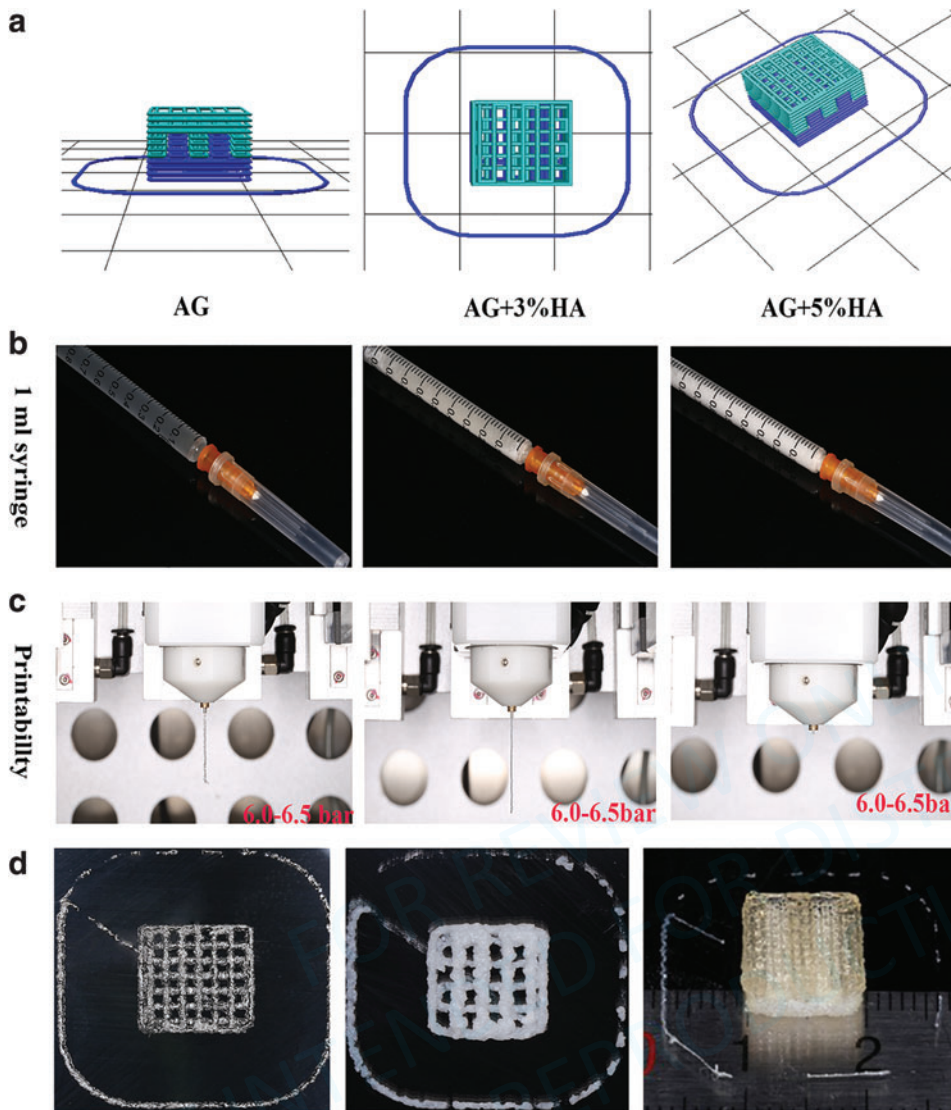
FIG. 2. **(a)** The lock-key cuboid model viewed from the *side* and *top* after slicing. **(b)** Macroscopic appearance of three bioinks with different concentration of nHA in 1 mL syringe. **(c)** The printability of three AG bioinks with different concentration of nHA under 6.0–6.5 bar. **(d)** AG and AG +3% nHA were extruded along the X–Y paths for the first layer, and the image of the 3D cell printed AG+GFs/AGH+BMSCs construct. AG, alginate/gelatin; AGH, alginate/gelatin/nano-hydroxyapatite. Color images are available online.

During the printing process, a 340 μm inner diameter cylindrical needle was applied for AG, while a 600 μm inner diameter cylindrical needle was applied for AG +3% nHA and AG +5% nHA. AG and AG +3% nHA could be extruded as filaments, while AG +5% nHA in 1 mL syringe could hardly be extruded under the pressure of 6.0–6.5 bar (Fig. 2c).

3D cell printing

A lock-key structure was designed using SOLIDWORKS 2018 to avoid discontinuity across the two regions and to strengthen cellular interaction at the interface. Before cell printing, the lock-key cuboid model with up and down structures was imported into the printer as stereolithography file and converted by MP Bioprint-v41 for slicing it into layers (Fig. 2a). There were 8 layers in the soft and hard region, respectively, with 4 embedded layers making up the lock-key structure, leading to the 12 layers of 3D printed soft-hard construct. Two types of cellular bioinks were then loaded aseptically into two 1 mL syringes (Table 1). At 30% and 25% infill for soft and hard regions, respectively, the bioinks were extruded along the X–Y paths for each layer and translated to Z paths at the end of one layer to create a $10 \times 10 \times 4\,mm^3$ cellular soft-hard construct (Fig. 2d).

After repeated printing tests, the parameters for cell printing presented in Table 2 were finally optimized to ensure consistency of the printing process and maximum cell viability with time. Ultimately, the construct was cross-linked with 50 mM sterilized $CaCl_2$ solution for 5–10 min at room temperature and then rinsed in PBS several times to remove residual $CaCl_2$ before culturing. After printing, it was suggested to transfer the construct into the culture medium as soon as possible. Twenty

TABLE 1. CELLULAR AND ACELLULAR BIOINK INGREDIENTS TO BIOPRINT THE SOFT-BONE CONSTRUCT

Bioinks	Alginate (%)	Gelatin (%)	nHA (%)	Cell ($3–4 \times 10^6$ cells/mL)	Printed position	Printed tissues
Cellular	2	8	—	GFs	Up	Soft
	2	8	3	BMSCs	Down	Hard
Acellular	2	8	—	—	Up	Soft
	2	8	3	—	Down	Hard

GFs, gingival fibroblast cells; BMSCs, bone marrow-derived mesenchymal stem cells; nHA, nano-hydroxyapatite.

TABLE 2. THE PRINTING PARAMETERS OF THE
EXTRUSION-BASED THREE-DIMENSIONAL BIOPRINTER

Parameters	Platform temperature (°C)	Storage temperature (°C)	Pressure (bar)	Speed (mm/s)	Needle gauge (G)
AG	15.0	24.5	2.0–2.5	10.0	23.0
AGH	15.0	22.5	2.5–3.0	8.0	20.0

AG, alginate/gelatin; AGH, alginate/gelatin/nano-hydroxyapatite.

percent fetal bovine serum was supplemented into the adequate medium to culture the 3D cell printed construct before the evaluation.

Physicochemical characterization

The compressive modulus of two constructs composed of AG and AGH was analyzed by applying a uniaxial compression force with a rate of 6.0 N/min using Dynamic Thermomechanical Analysis (TA) at room temperature. The compressive modulus was calculated from the slope of the linear elastic region of the stress–strain curve, which was between 5% and 15% deformation for all samples.

Chemical components of AG and AGH hydrogels were analyzed using an Attenuated Total Reflectance-Fourier Transform Infrared Spectroscopy (ATR-FTIR; Bruker, Germany) in the range from 600 to 4000 cm^{-1} with a resolution of 4 cm^{-1}. Each sample was directly analyzed on an ATR accessory equipped with a diamond crystal. The number of scans was 32. Crystal phase compositions of AGH that were measured by X-ray diffraction spectroscopy (XRD; Bruker, Germany) used the setup of nickel-filtered Cu Kα radiation at 40 kV and 40 mA. The diffraction spectra were recorded with a scanning speed of 0.2°/s and a step size of 0.02° in the range of 2θ between 5° and 90°. The construct was ground into powder after lyophilized to test its chemical components and crystal phase compositions.

The rheological characterization was measured by the viscosity at 25°C, when the shear rate varied from 0.01 to 100 s^{-1} using HAAKE Mars 40 Rheometer (Thermos Electron GmbH, Karlsruhe, Germany).

The degradation of AG and AGH hydrogels was also measured. Cubes measuring $10 \times 10 \times 4$ mm^3 with 30% infill were printed using AG, while $10 \times 10 \times 4$ mm^3 cubes with 25% infill were printed using AGH. After cross-linking, samples were placed in a 12-well plate and immersed in PBS. During the 8-week observation, PBS was changed every 2 days. Each sample was lyophilized for 3–4 h before weighing at days 0, 3, 7, 14, 21, 28, 42, and 56. Dry weight at each time was recorded (W_1). The mass loss (ML) was calculated by the equation listed below: (W_0: dry weight at day 0)

$$ML = \frac{W_0 - W_1}{W_0} \times 100\%$$

All physicochemical experiments were conducted in triplicate.

Morphology observation by scanning electron microscopy

Macroscopic morphology of the construct and cell morphology on the construct were observed using a scanning electron microscopy (SEM, Quanta 200, Netherlands). Four

percent paraformaldehyde for 10–15 min was necessary to fix the encapsulated cell. After that, the sample was lyophilized and mounted on aluminum stubs and sputter coated with gold–palladium before analysis. Construct morphology and cell adhesion were examined at an accelerated voltage of 5–20 kV.

Cell viability assay

Cell viability in two constructs composed of AG and AGH was analyzed using a Live/Dead Viability Kit (KGAF001; KeyGEN Bio-TECH, China). Before the Live/Dead assay, each construct was cross-linked with 50 mM sterilized CaCl$_2$ for 5–10 min at room temperature. It was then incubated in 8 µM propidium iodide and 2 µM Calcein-AM (dispensed in PBS) for 25 min. The sample was visualized using Confocal Microscopy (Leica TCS, SP8, Germany) after three consecutive washes with PBS. 3D images were generated after scanning 8 mm × 8 mm × 440 µm stack of each construct, and the cell viability in each group was quantified using Image J analysis from three different samples.

Cell proliferation analysis

Cell Counting Kit-8 (CCK-8; Dojindo, Japan) was applied for cell proliferation analysis at days 1, 3, 5, and 7 after printing. After incubation for 2 h at 37°C, the supernatant was harvested into a 96-well plate, and the optical density (OD) was measured at 450 nm using a Microplate Reader (ELx800, Biotek). Constructs without cells were used as the control ($n = 3$).

Quantitative reverse transcription-polymerase chain reaction analysis of gene expression

By applying quantitative reverse transcription-polymerase chain reaction (qRT-PCR), the transcriptional levels of appropriate genes in GFs and BMSCs were quantified at days 7 and 14 in the construct. To release the encapsulated cells, constructs were transferred into 2 mL of 55 mM Na-citrate for 5 min at 37°C, and then the cells were collected by centrifugation at 1000 rpm for 10 min.

Total RNA was extracted using the TRIzol Reagent (Invitrogen) according to the manufacturer's recommended protocol. PrimeScript™ RT Reagent Kit (TaKaRa, Japan) was applied for reverse transcription, and FastStart Universal SYBR Green Master (Roche, Germany) was used for qRT-PCR. In GFs, the expression level of *COL-I* was quantified, while *ALP*, *OCN*, and *RUNX-2* were assessed in BMSCs using the primers listed in Table 3. *GAPDH* served as a normalization control, and fold differences were calculated by the $2^{-\Delta\Delta Ct}$ method ($n = 3$).

In vivo *study*

According to ethical principles of the Peking University Institutional Animal Care and Use Committee (License No. LA2020006), the constructs were inserted subcutaneously into the dorsum of 6- to 8-week-old male BALB/c nude mice to verify the biocompatibility of this 3D cell printed construct. Animals were fed in two individually ventilated cages in a barrier SPF unit 1 week before the study. A single animal was considered as an experimental unit. The implants were divided into two groups: the cell printed AG+GFs/AGH+BMSCs group and the acellular printed AG/

TABLE 3. PRIMERS FOR TRANSCRIPTION FACTORS FOR *GAPDH, COL-I, ALP, RUNX*-2, AND *OCN*

Gene	Primes
GAPDH	F: CGGACCAATACGACCAAATCCG
	R: AGCCACATCGCTCAGACACC
COL-1	F: CAAGA TGTGCCACTCTGACT
	R: TCTGACCT GTCTCCATGTTG
ALP	F: ATGGGATGGGTGTCTCCACA
	R: CCACGAAGGGGAACTTGC
RUNX-2	F: CCGCCTCAGTGATTTAGGGC
	R: GGGTCTGTAATCTGACTCTGTCC
OCN	F: CACTCCTCGCCCTATTGGC
	R: CCCTCCTGCTTGGACACAAAG

AGH group as the control. Taking the Reduction principle into account, five nude mice were used in each group to ensure the reproducibility and reliability of data obtained from the animal model.

All instruments used were sterilized by Co-60, and the surgery was carried out in the clean bench with infection control. Six- to eight-week-old male BALB/c nude mice (Vital River, approximately 20–25 g, $n = 10$) were divided into two groups with the principle of simple randomization and anesthetized with 4% chloral hydrate (100 μL/10 g). Two percent lidocaine hydrochloride for local anesthesia was supplied to alleviate postoperative pain. The soft region consisting of AG+GFs or AG was positioned externally, while the bone region with AGH+BMSCs or AGH was placed in contact with muscle. After the surgery, animals rewarmed on a warming pad and then returned to the cages for further observation. Sterilized jelly and egg yolk were supplemented during the first 3 days after the surgery to promote wound healing.

Animals were sacrificed with an overdose injection of chloral hydrate at weeks 4 and 8. Subcutaneous constructs were retrieved and fixed in 4% formalin fixative, dehydrated, and embedded in optimal cutting temperature compound. After that, the constructs were sectioned to a thickness of 4–6 μm with the mineral component preserved for hematoxylin and eosin (HE) staining, while constructs at week 8 were also sectioned for Masson trichrome staining. Histomorphometry was conducted in terms of the report from the ASBMR Histomorphometry Nomenclature Committee.[26] The fiber density was measured using ImageJ, and blood vessels were counted to semiquantify the different performance between the cell printed construct and the acellular printed construct.

To better illustrate the performance of BMSCs and GFs *in vivo*, GFs and BMSCs were fluorescently labeled using LV10N-NC and LV3-NC lentiviruses (GenePharma Co., Shanghai, China), respectively. After that, cells were mixed with the hydrogel in preparation for cell printing. Constructs were kept in the dark in the dorsum of nude mice and imaged at weeks 2 and 4 postimplantation. From the macroscopic view, live *in vivo* imaging was performed to monitor the viability of implanted cell using Small Animal Fluorescence Imaging System CRI (Maestro2, Xenogen). Then, the animals were sacrificed, and the implants were retrieved to visualize the fluorescent-labeled cell performance under the Confocal Microscopy.

There were three different experimenters dominating the surgery operation, the outcome assessment, and the data analysis, respectively.

Statistical analysis

Data were expressed as mean ± standard deviation of experiments performed in triplicate and analyzed using SPSS 20.0 software. *T*-test and one-way analysis of variance (ANOVA) were performed for statistical analysis. A *p*-value lower than 0.05 was determined as statistically different.

Experiment

Bioink characterization

Mechanical characterization. The mechanical testing indicated that predesigned lock-key construct composed of AG and AGH withstood normal mechanical loading. As seen in Figure 3c, compared with AG (43.74 ± 2.69 KPa), the addition of nHA improved the compressive modulus (61.62 ± 3.42 KPa).

Attenuated Total Reflectance-Fourier Transform Infrared Spectroscopy analysis. In the ATR-FTIR spectra (Fig. 3a), the peak at 3291.90 cm^{-1} was ascribed to the OH$^-$ stretching vibration, while the peak at 1643.64 cm^{-1} arose from the C=O absorption of Amide I. The peak at 1122.98 cm^{-1} was associated with the major bond of SO_4^{2-} in gelatin. In addition, the peak at 2934.88 cm^{-1} was attributed to CH$_2$ stretching vibrations, while 1085.39 and 1084.30 cm^{-1} signals were the result of CH stretching vibrations. The AG and AGH hydrogel displayed analogous peaks associated with alginate/gelatin. The peak at 1030.74 cm^{-1} observed for AGH was ascribed to the PO_4^{3-} absorption of nHA, which was not present in the spectrum of AG.

X-ray diffraction spectroscopy analysis. The XRD pattern of AGH presented in Figure 3e revealed diffraction peaks at $2\theta = 25.8°$, 31.8°, 32.9°, corresponding to the characteristic diffraction pattern of nHA added in the AGH hydrogel. The degree of crystallinity of nHA and AGH was characterized using the fundamental parameter approach[27] and was estimated to be 59.9% and 52.6%, respectively.

Rheological characterization. The viscosity of both AG and AGH hydrogel had a descending trend with increasing shear rate within certain scope, indicating that AG and AGH hydrogels have proper viscosity. The viscosity was increased after adding nHA compared with the AG hydrogel (Fig. 3d).

Degradation rate analysis *in vitro*. Figure 3b showed that two constructs composed of AG and AGH degraded over time. The addition of nHA made this degradation slowdown in comparison to the AG construct in the 8-week observation ($p < 0.01$). At day 7, the ML of the AG construct was about 52.1%, while the ML of the AGH construct was 33.2%. At day 28, 90.9% AG degraded, and only some amorphous residue was left. However, the ML of the AGH construct was 64.7% at day 28, and the AGH construct still maintained its grid-like structure. At day 56, the ML of the AGH construct was 89.6%.

Scanning electron microscopy analysis (SEM). The grid-like inner structure of this 3D printed construct was presented in Figure 4a and b. The pore diameters for the soft
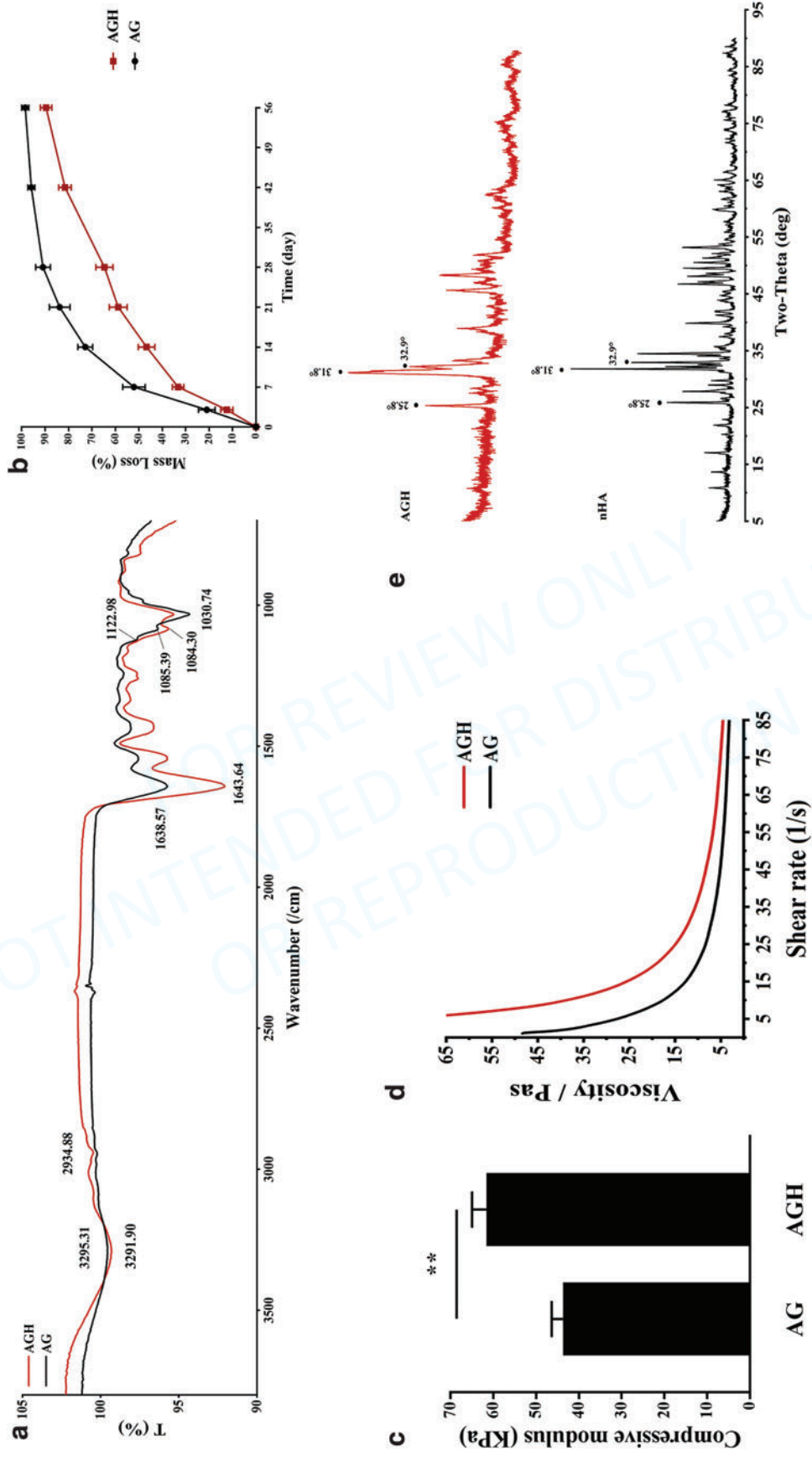
FIG. 3. Physicochemical characterization of AG and AGH. (**a**) ATR-FTIR analysis. (**b**) The degradation rate of AG and AGH during 8-week observation. (**c**) Compressive modulus of AG and AGH. (**d**) The viscosity of AG and AGH. (**e**) XRD analysis. The *black dots* in AGH and nHA indicate the main peaks of the $Ca_{10}(PO_4)_6(OH)_2$ phase (No. 01-084-1998 in the International Center for Diffraction Data). Data are presented as mean ± standard deviation, $n = 3$; **Statistical difference at $p < 0.01$. ATR-FTIR, attenuated total reflectance-Fourier transform infrared spectroscopy; XRD, X-ray diffraction spectroscopy. Color images are available online.
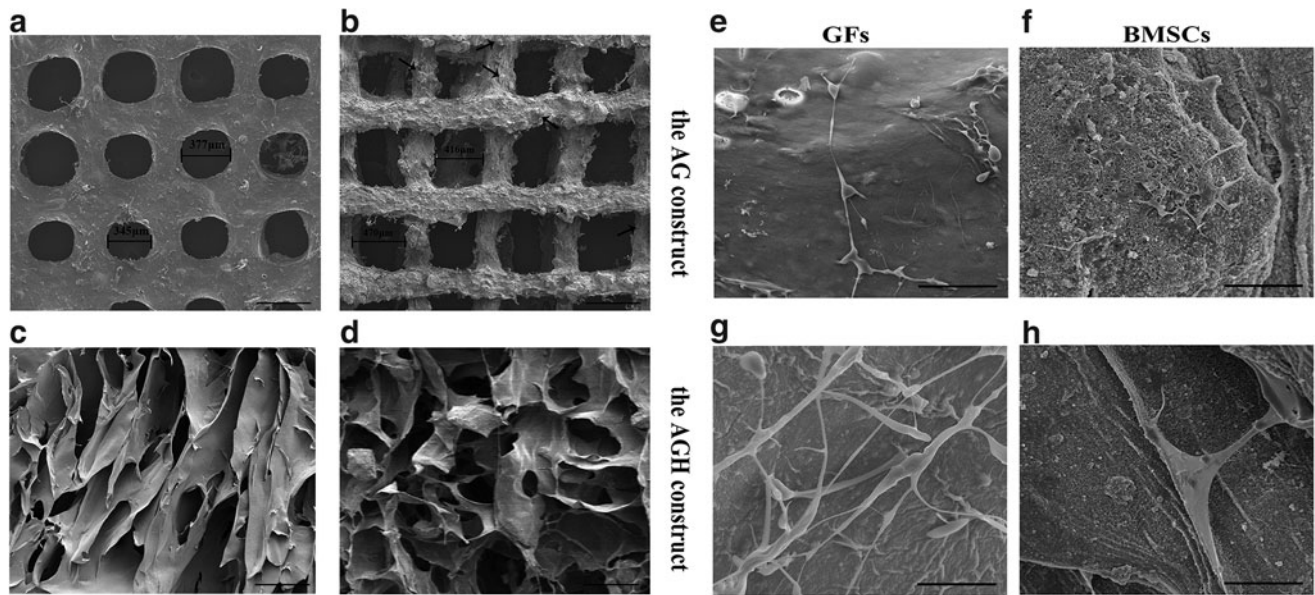
FIG. 4. **(a)** The SEM image of the grid-like inner structure in the soft region. The pore diameter was ~300 μm. **(b)** The SEM image of the grid-like inner structure in the hard region. The pore diameter was ~400 μm. The *black arrows* indicate the deposited nHA. Scale bar: 500 μm. The SEM images of microstructure in **(c)** the soft and **(d)** the hard region. The pore size was about 30–200 μm. Scale bar: 100 μm. **(e–h)** The SEM images of cell morphology on the construct. GFs and BMSCs stretched and attached well at day 14 postprinting. Scale bar: 50 μm for **(e, f)** and 20 μm for **(g, h)**. SEM, scanning electron microscopy.

region (composed of AG) and hard region (composed of AGH) were ~300 and 400 μm, respectively. The micropore size of the soft and hard region was in the range 30–200 μm (Fig. 4c, d). nHA was successfully deposited and spherically distributed on the surface, which made the surface of the hard region rougher compared with the soft region.

Cell morphology on the construct

Cell morphology on the construct was observed by SEM in the four groups at day 14 postprinting. As seen in Figure 4e and f, both GFs and BMSCs stretched and attached to the surface of the AG construct. Upon the addition of nHA, both cell types became elongated and homogenous, exhibiting a high degree of cell connectivity (Fig. 4g, h). The appearance of GFs resembled a typical fibrous shape compared with that of BMSCs.

Cell viability (Live/Dead) assay

Figure 5a and b illustrated the cell Live/Dead images in the four groups. Dead cells were distributed uniformly in the constructs at day 3, while at day 7 their distribution was more localized. Cell viability in all four groups increased over time. The data presented in Figure 5c showed that GFs' viability was consistently higher compared with BMSCs. Upon addition of nHA, BMSCs' viability at both day 3 (71.99% ± 1.57%) and day 7 (86.59% ± 0.75%) decreased compared with the AG+BMSCs group (75.19% ± 1.30% at day 3 and 89.29% ± 0.80% at day 7). The GFs' viability was lower in the AGH group (81.32% ± 1.10%) than in the AG group (87.75% ± 0.97%) at day 3; at day 7, GFs' viability in AG constructs reached to 94.80% ± 1.14%, which was higher than that observed in AGH constructs (92.47% ± 0.77%).

Cell proliferation assay

The cell proliferation result indicated an upward trend during 7 days of culture in the four groups (Fig. 5d, e). At day 7, two GF groups exhibited higher OD values compared with two BMSC groups. The highest proliferation rate was observed between days 5 and 7 in all four groups.

Gene expression analysis

As seen in Figure 6a, a higher expression level of *COL-I* in GFs was observed in AGH constructs compared with AG constructs. However, the expression level of *COL-I* in both AG and AGH constructs decreased with time.

The expression levels of osteogenic gene markers in BMSCs (*ALP*, *RUNX-2*, and *OCN*) in OM were enhanced compared with those in parallel PM and increased over time, reaching a maximum at day 14 (Fig. 6b–d). In the parallel PM groups, the expression levels of three osteogenic gene markers in AGH constructs were 1–2 times higher than those in AG constructs. In the OM groups, the fold increases (compared with PM groups) of *ALP*, *RUNX-2*, and *OCN* were 1–3 times higher in AGH constructs than those in AG constructs.

In vivo *experiments*

Constructs were harvested at weeks 4 and 8 following implantation with no exclusions ($n = 5$ for each group). The residual construct volume in both acellular printed AG/AGH group (Fig. 7a) and cell printed AG+GFs/AGH+BMSCs (Fig. 7e) group was smaller than the preimplantation volume. The acellular printed construct was more irregular and fragile compared with the cell printed construct. The surface of the soft region was smooth and soft in texture, while the surface of the hard section appeared resilient and rough in texture.
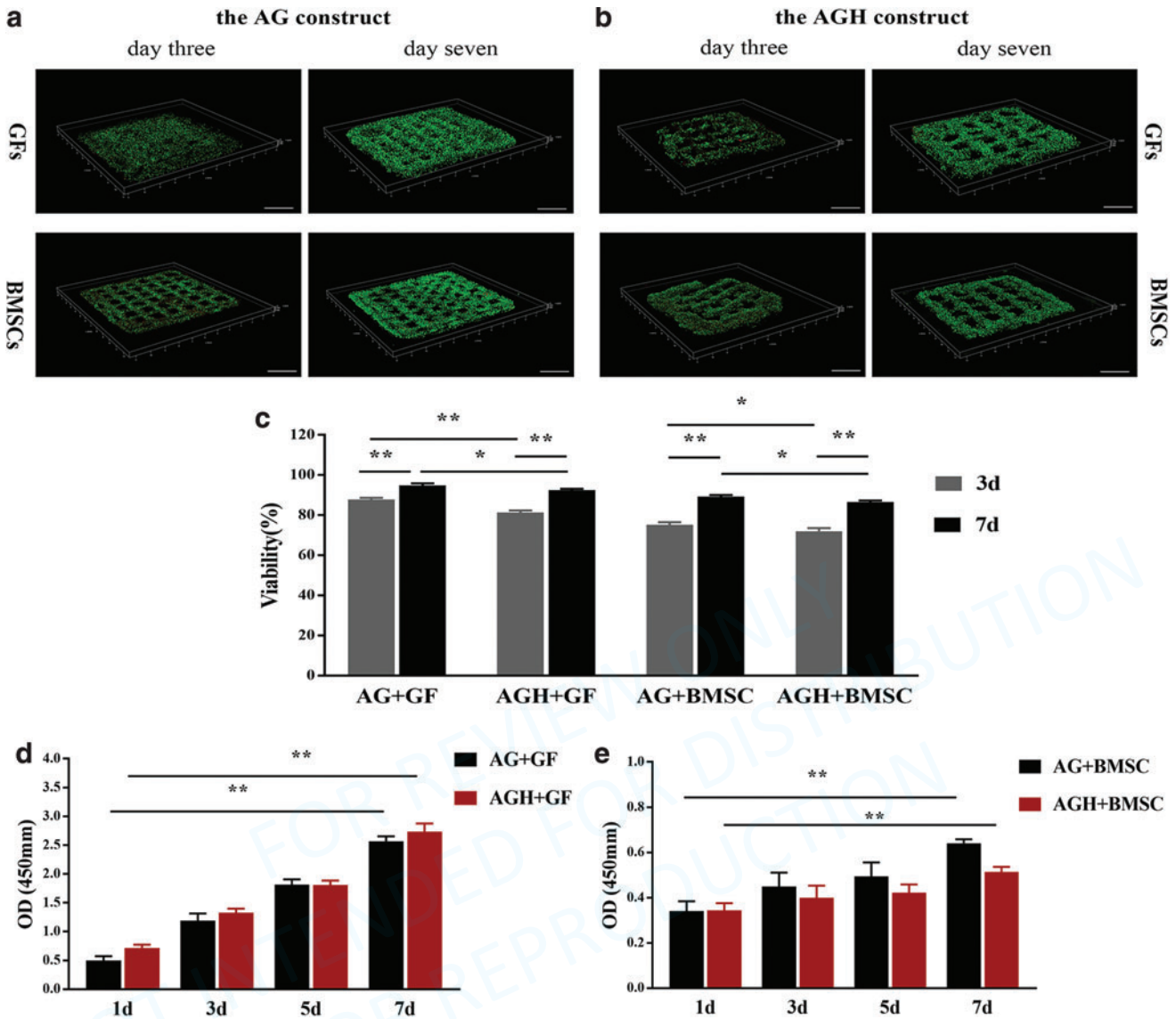
FIG. 5. Live/Dead assay and the proliferation of GFs and BMSCs in AG and AGH constructs. Live/Dead assay of GFs and BMSCs **(a)** in AG and **(b)** AGH constructs at days 3 and 7. Scale bar: 2 mm; living and dead cells are displayed in *green* and *red*, respectively. **(c)** Cell viability of the above four groups at days 3 and 7. The proliferation of **(d)** GFs in AG and AGH constructs and **(e)** BMSCs in AG and AGH constructs at days 1, 3, 5, and 7 postprinting. Data are presented as mean ± standard deviation, $n = 3$; *Statistical difference at $p < 0.05$; **Statistical difference at $p < 0.01$. 3d, day 3; 7d, day 7; AG+GF, GFs encapsulated in the construct composed of alginate/gelatin; AGH+GF, GFs encapsulated in the construct composed of AGH; AG+BMSC, BMSCs encapsulated in the construct composed of alginate/gelatin; AGH+BMSC, BMSCs encapsulated in the construct composed of AGH. Color images are available online.

The cross-sectional views of the acellular printed construct (Fig. 7b, c) and the cell printed (Fig. 7f, g) construct were observed by HE staining. Porous grids, nHA nodes, and vascular distribution could be partially observed in both the groups without inflammatory responses.

At week 4, more vascular distribution was observed in the cell printed construct than that in the acellular construct, and the former group exhibited better healing in upper subcutaneous tissue ($p < 0.01$). At week 8, differences in the inner structure of constructs and behavior of subcutaneous tissue were observed: (1) structure of the acellular printed construct broke down, while the cell printed construct maintained as integrated. (2) In the cell printed group, subcutaneous tissue close to the printed construct was dense

and orderly, while the subcutaneous layer was loose in the acellular printed group. (3) In the cell printed construct, osteoblasts were found in the bone region, especially in the vicinity of nHA nodes. (4) By Masson staining (Fig. 7d, h), the cell printed construct was stained as deep red, which was probably caused by mineralized extracellular matrix.[28]

From Figure 7i and j, there were statistically significant differences in the fiber density of the subcutaneous tissue and the number of vessels between the cell printed construct and the acellular printed construct.

In Figure 8, green fluorescent protein-labeled BMSCs and red fluorescent protein-labeled GFs could be detected during the 4-week implantation. What's more, the cell density increased at week 4 (Fig. 8i, l) compared with week 2 (Fig. 8c, f).
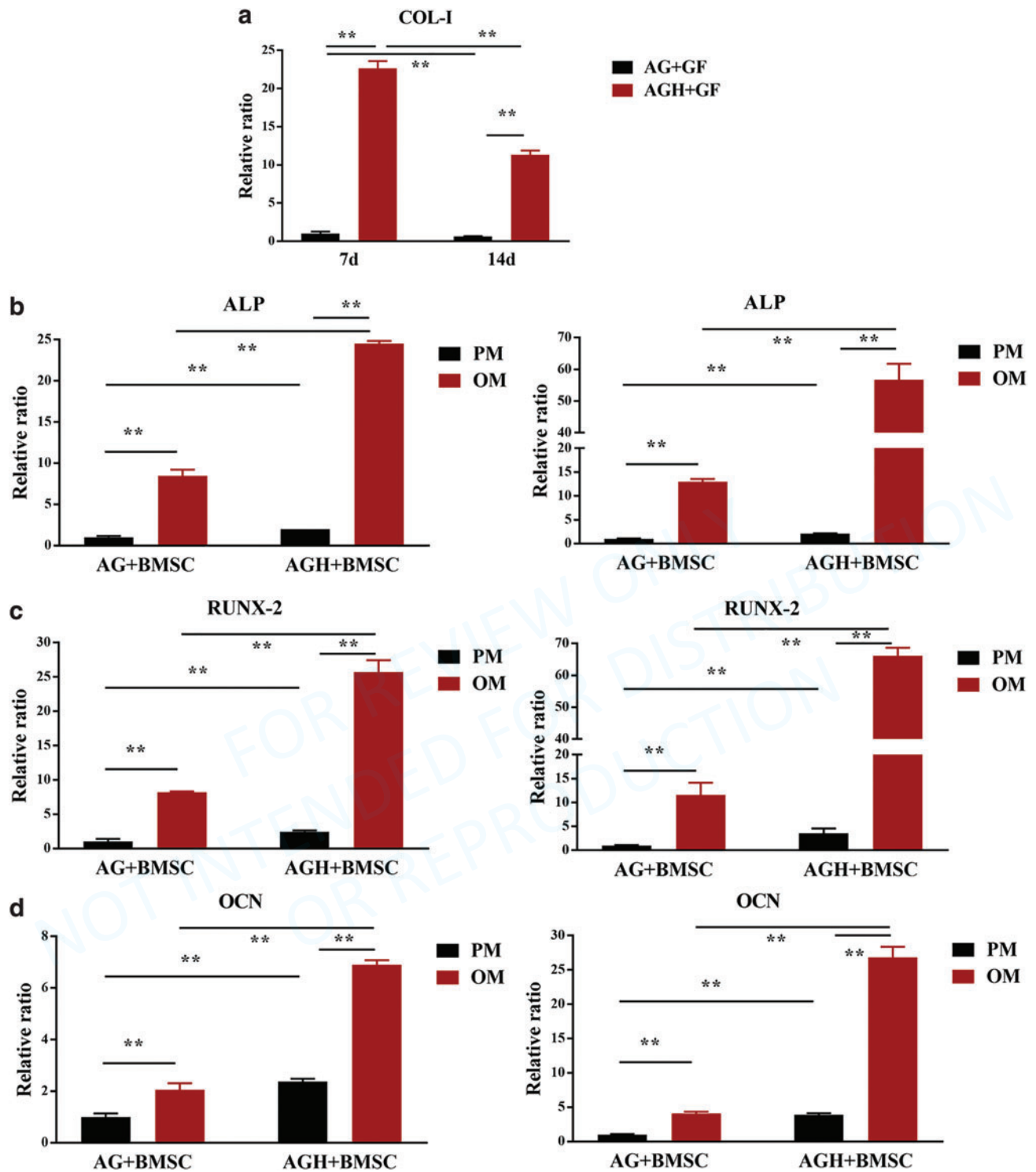
FIG. 6. Quantitative gene expression levels of **(a)** *COL-I* in GFs at days 7 and 14 in AG and AGH constructs. The expression levels of **(b)** *ALP*, **(c)** *RUNX-2*, and **(d)** *OCN* in BMSCs at days 7 (*left*) and 14 (*right*) after culturing in OM and PM in AG and AGH constructs, respectively. The y-axis represents the relative ratio of related gene expression normalized to *GAPDH*. Data are presented as mean ± standard deviation, $n = 3$; **Statistical difference at $p < 0.01$. OM, osteogenic medium; PM, proliferation medium. Color images are available online.
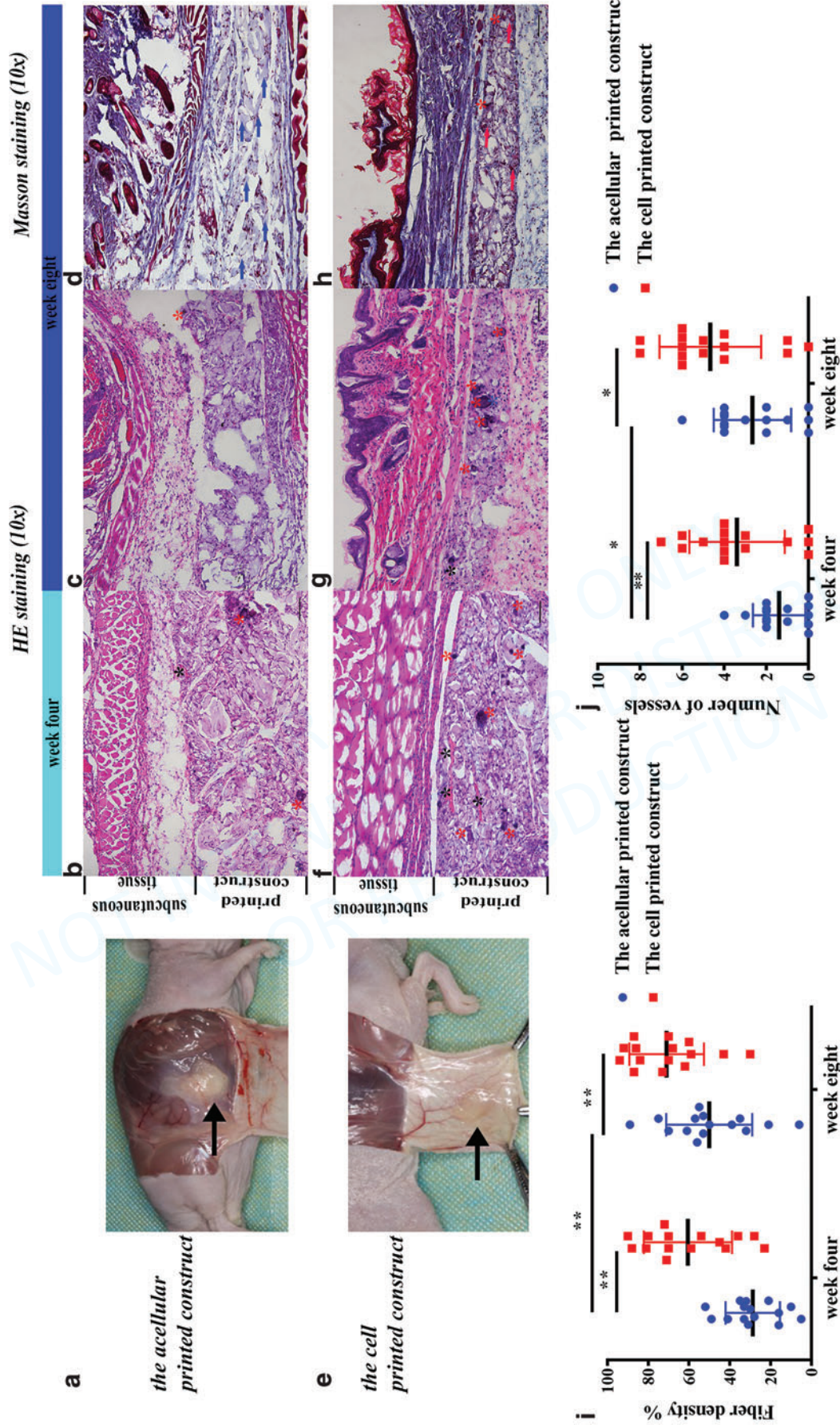
FIG. 7. *In vivo* experiments: scale bar: 100 μm. (**a**) The acellular printed AG/AGH construct and (**e**) the cell printed AG+GFs/AGH+BMSCs construct were harvested after implantation (indicated by the *black arrow*). According to the HE staining (**b, c, f, g**), nHA nodes (indicated by the *red asterisk*) and vascular distribution (indicated by the *black asterisk*) were identified. Osteoblasts around the HA nodes were observed in the cell printed constructs at week 8 (indicated by the *blue asterisk*). By Masson staining at week 8, (**d**) the acellular printed AG/AGH construct was stained as *blue* (indicated by the *blue arrow*), while (**h**) the cell printed construct was stained as deep *red* (indicated by the *red arrow*). Semiquantitative analysis of the cell printed construct in comparison with the acellular printed construct based on the (**i**) fiber density in the subcutaneous tissue and (**j**) vascular distribution. Date are presented as mean ± standard deviation, $n = 5$ animals, $n = 3$ slices per animal; *Statistical difference at $p < 0.05$; **Statistical difference at $p < 0.01$. HE, hematoxylin and eosin. Color images are available online.
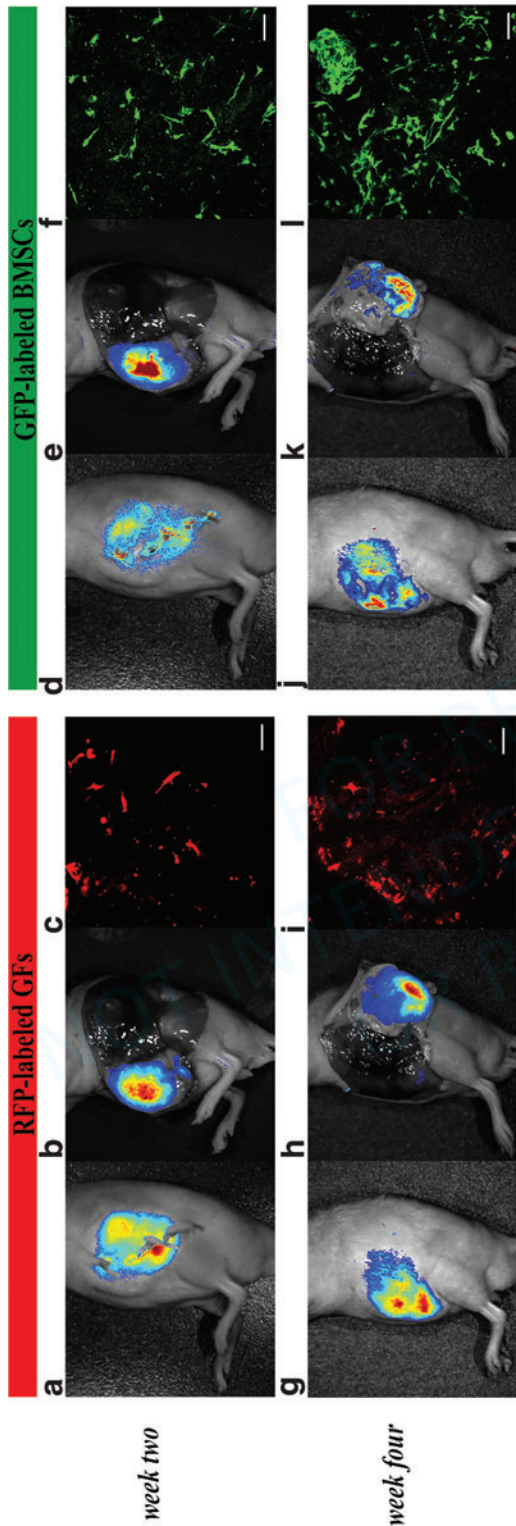
10

FIG. 8. Fluorescent cell labeling and tracking *in vivo* during 4-week implantation. Live *in vivo* imaging was performed to observe (**a, b, g, h**) the RFP-labeled GFs and (**d, e, j, k**) the GFP-labeled BMSCs *in situ*. The morphologies of (**c, i**) GFs and (**f, l**) BMSCs were visualized under the confocal microscopy. Scale bar: 100 μm. RFP, red fluorescent protein; GFP, green fluorescent protein. Color images are available online.

Discussion

With recent advancements in tissue engineering, creating a heterogeneous construct to regenerate the oral soft and hard defects becomes possible but remains challenging.[29] Although multilayered 3D bioprinted scaffolds have achieved some successful outcomes, the lack of scalability and cell organization may attribute to the surgical failure in an attempt to repair the lost periodontal tissue.[30–32] Hence, it is clinically relevant to design a heterogeneous construct that can not only bear patient-specific geometries but also maintain functional integration with distinct features (e.g., soft and hard tissues).

With a more accurate spatial control, 3D cell printing is now capable of engineering a highly anisotropic structure with zonal biomechanical properties in the articular cartilage field.[33] Idaszek *et al.* have used articular chondrocytes and BMSCs dispersed into two hydrogels to bioprint a hyaline-calcified cartilage construct, and results suggested long-term and functional cell survival and the formation of zone-specific matrices.[34] The special anatomy of the tooth extraction socket provides a stable and favorable condition for soft-hard tissue regeneration, which is advantageous to the clinical transformation in the future. Therefore, using 3D cell printing for alveolar soft-hard tissue engineering is promising these days.[22,35]

In this study, we set out to design a lock-key heterogeneous construct to promote soft-tissue healing and hard-tissue regeneration by 3D cell printing. Physicochemical and biological properties (viability, proliferation, and osteogenic differentiation) all suggested that the 3D cell printed lock-key structure had potential for further clinical studies in soft-hard regeneration in alveolar process.

The demand to maintain cell viability in 3D printed constructs limits the application of biomaterial. The hydrogel used in this study belongs to a class of naturally derived polymers, which have been widely implemented in 3D cell printing due to their similarity to extracellular matrix and hydrophilic properties. Nonetheless, alginate lacks cell-adhesive ligands, which can be improved by adding gelatin—a thermoresponsive hydrogel containing built-in ligands and an arginine-glycine-aspartic acid (RGD) peptide.[36–38] When culturing in the medium at 37°C, a part of gelatin tends to leach out from the mixed gel, contributing to the porous microstructure in the construct.

The desired construct needs to provide micropores for vasculature and matrix. The porous microstructure of the printed filaments can facilitate cellular infiltration and microvascularization in the construct, thereby promoting survival and integration.[39] Moreover, the porous biomaterial with a spongy-bone like structure promotes the osteoconductivity while minimizing fibrotic encapsulation.[40]

As alginate is ion-sensitive, ionic cross-linking agents such as Ca^{2+} can transform an aqueous alginate solution into a gel.[41–43] Data from our previous studies suggested that a blend of 2 wt% alginate and 8 wt% gelatin cross-linked by 50 mM $CaCl_2$ for 5 min was good for bioink preparation.[44] Besides that, Zhang *et al.* found that soft scaffold with low concentration of alginate was better for osteogenic differentiation of stem cells than stiff scaffolds with high concentration of alginate.[45] Thus, 2 wt% alginate and 8 wt% gelatin were used to encapsulate cells in this study. Two kinds of bioinks (GFs in AG and BMSCs in AGH) were loaded and extruded through two needles at 22–25°C.

Considering the increase in viscosity and consequently nozzle clogging upon the addition of nHA,[46] a smaller needle gauge was necessary for printing the AGH bioink. To achieve good printability, nHA was stored at a dry environment to avoid forming liquid bridge between particles. Ultrasonic and mechanical agitation was applied in turn during the preparation of the AGH hydrogel. Owing to a relatively low concentration of nHA added and methods used above, the AGH hydrogel composed of 3% nHA was extruded fluently. However, the concomitant rise in shear stress and dispensing pressure could lead to a decrease in cell viability.[47,48] At day 3 after printing with AGH, GFs' viability decreased to 81.32%±1.10% and BMSCs' viability was 71.99%±1.57%. Adequate porosity, proper parameters during the cell printing, and optimum culture condition make sense to maintain cell viability in the 3D cell printed construct.

The physicochemical characterization of AG and AGH hydrogel demonstrated that the AG hydrogel was composed of alginate/gelatin, while additional nHA existed in the AGH hydrogel. The lower degree of crystallinity in AGH than nHA is likely due to the addition of the amorphous alginate/gelatin. According to a previous report, HA promoted the mechanical properties of a freeze-dried molding scaffold.[49] In this study, the addition of 3% nHA into the AG hydrogel not only contributed to an increase in mechanical properties but also slowed down the degradation rate, which was helpful for osteogenic differentiation of BMSCs.

In cell studies, SEM images demonstrated adequate attachment of both GFs and BMSCs on the 3D printed construct. Specifically, the construct containing nHA performed better than the AG construct, as it presented a rough substrate for cell attachment. CCK-8 result showed that cell proliferation of BMSCs slowed down in the AGH construct compared with the AG construct, which could be partly caused by the nHA added.[50] As confirmed by PCR analysis, nHA could promote the osteodifferentiation of BMSCs. Besides that, the enhanced expression of *COL-I* in GFs was found in the AGH construct, which could be partially due to the high cell connectivity establishing on the AGH construct according to the SEM images. However, a decrease in the expression of *COL-I* was observed at day 14 compared with day 7, which probably indicated increased cell migration, which could temporarily suppress proliferation.[51,52]

Finally, the implantations were harvested from nude mice at weeks 4 and 8. Both acellular and cell printed constructs were observed without the presence of inflammation, indicating their positive effects on microenvironment provision.[53–55] In the cell printed construct, more integrated structure and vascular distribution were observed, which could be partly due to cells encapsulated in the constructs.[56,57] At week 8, osteoblasts were found around nHA in the cell printed construct, and the construct was stained deep red by Masson, indicating the better ability to form new mineralized extracellular matrix. Although bilayer structure was not apparent in both the groups, dense and mature subcutaneous tissue close to the cell printed group indicated the better ability to promote subcutaneous tissue healing.

By tracking the encapsulated cell *in vivo*, the result further demonstrated that GFs and BMSCs could maintain survival and proliferation in the soft and hard region, respectively, indicating the good biocompatibility of this 3D cell printed construct.

From above, GFs and BMSCs maintained their cell viability, proliferation, and function in this integrated and heterogeneous soft-hard construct. The difficulties of developing an integrated construct with heterogeneity and ensuring its dual function were overcome in this study.

Conclusion

An integrated and heterogeneous soft-hard construct was successfully assembled as a lock-key structure by 3D cell printing, and it was confirmed that this soft-hard construct composed of AG/GFs (soft) and AGH/BMSCs (hard) could maintain cell viability and functional differentiation of GFs and BMSCs according to their desired characterization. These preliminary results indicate that the 3D printed soft-hard construct could promote soft-tissue healing and hard-tissue regeneration. This 3D printed soft-hard construct has the potential to be a customized plug in alveolar ridge preservation.

Authors' Contributions

Q.L. and S.Z. contributed to the conception and design of the work. S.Z. and P.L. collected the data; S.Z. and C.L. analyzed the data; S.Z. designed the schematic illustrations; and S.Z., Q.L., and H.-L.W. led the writing.

Disclosure Statement

No competing financial interests exist.

Funding Information

References

1. Tan, W.L., Wong, T.L.T., Wong, M.C.M., and Lang, N.P. A systematic review of post-extractional alveolar hard and soft tissue dimensional changes in humans. Clin Oral Implants Res **23(Suppl 5),** 1, 2012.

2. Zhao, L., Wei, Y., Xu, T., Zhang, B., Hu, W., and Chung, K.-H. Changes in alveolar process dimensions following extraction of molars with advanced periodontal disease: a clinical pilot study. Clin Oral Implants Res **30,** 324, 2019.

3. Van der Weijden, F., Dell'Acqua, F., and Slot, D.E. Alveolar bone dimensional changes of post-extraction sockets in humans: a systematic review. J Clin Periodontol **36,** 1048, 2009.

4. Lee, J., Lee, J.B., Koo, K.T., Seol, Y.J., and Lee, Y.M. Flap management in alveolar ridge preservation: a systematic review and meta-analysis. Int J Oral Maxillofac Implants **33,** 613, 2018.

5. Lim, H.-C., Shin, H.-S., Cho, I.-W., Koo, K.-T., and Park, J.-C. Ridge preservation in molar extraction sites with an open-healing approach: a randomized controlled clinical trial. J Clin Periodontol **46,** 1144, 2019.

6. Guo, T., Lembong, J., Zhang, L.G., and Fisher, J.P. Three-dimensional printing articular cartilage: recapitulating the complexity of native tissue. Tissue Eng Part B Rev **23,** 225, 2017.

7. Weems, A.C., Pérez-Madrigal, M.M., Arno, M.C., and Dove, A.P. 3D printing for the clinic: examining contemporary polymeric biomaterials and their clinical utility. Biomacromolecules **21,** 1037, 2020.

8. Ozler, S.B., Bakirci, E., Kucukgul, C., and Koc, B. Three-dimensional direct cell bioprinting for tissue engineering. J Biomed Mater Res B Appl Biomater **105,** 2530, 2017.

9. Choe, G., Oh, S., Seok, J.M., Park, S.A., and Lee, J.Y. Graphene oxide/alginate composites as novel bioinks for three-dimensional mesenchymal stem cell printing and bone regeneration applications. Nanoscale **11,** 23275, 2019.

10. Chae, S., Lee, S.S., Choi, Y.J., *et al.* 3D cell-printing of biocompatible and functional meniscus constructs using meniscus-derived bioink. Biomaterials **267,** 120466, 2021.

11. Gillispie, G., Prim, P., Copus, J., *et al.* Assessment methodologies for extrusion-based bioink printability. Biofabrication **12,** 022003, 2020.

12. Kang, H.W., Lee, S.J., Ko, I.K., Kengla, C., Yoo, J.J., and Atala, A. A 3D bioprinting system to produce human-scale tissue constructs with structural integrity. Nat Biotechnol **34,** 312, 2016.

13. Afjoul, H., Shamloo, A., and Kamali, A. Freeze-gelled alginate/gelatin scaffolds for wound healing applications: an *in vitro*, *in vivo* study. Mater Sci Eng C Mater Biol Appl **113,** 110957, 2020.

14. Chen, Q., Tian, X., Fan, J., Tong, H., Ao, Q., and Wang, X. An interpenetrating alginate/gelatin network for three-dimensional (3D) cell cultures and organ bioprinting. Molecules **25,** 756, 2020.

15. Augst, A.D., Kong, H.J., and Mooney, D.J. Alginate hydrogels as biomaterials. Macromol Biosci **6,** 623, 2006.

16. Cross, L.M., Thakur, A., Jalili, N.A., Detamore, M., and Gaharwar, A.K. Nanoengineered biomaterials for repair and regeneration of orthopedic tissue interfaces. Acta Biomater **42,** 2, 2016.

17. El-Meliegy, E., Abu-Elsaad, N.I., El-Kady, A.M., and Ibrahim, M.A. Improvement of physico-chemical properties of dextran-chitosan composite scaffolds by addition of nano-hydroxyapatite. Sci Rep **8,** 12180, 2018.

18. Chiesa, I., De Maria, C., Lapomarda, A., *et al.* Endothelial cells support osteogenesis in an *in vitro* vascularized bone model developed by 3D bioprinting. Biofabrication **12,** 025013, 2020.

19. Holmes, B., Bulusu, K., Plesniak, M., and Zhang, L.G. A synergistic approach to the design, fabrication and evaluation of 3D printed micro and nano featured scaffolds for vascularized bone tissue repair. Nanotechnology **27,** 064001, 2016.

20. Li, Q., Lei, X., Wang, X., Cai, Z., Lyu, P., and Zhang, G. Hydroxyapatite/collagen three-dimensional printed scaffolds and their osteogenic effects on human bone marrow-derived mesenchymal stem cells. Tissue Eng Part A **25,** 1261, 2019.

21. Bas, O., De-Juan-Pardo, E.M., Meinert, C., *et al.* Biofabricated soft network composites for cartilage tissue engineering. Biofabrication **9,** 025014, 2017.

22. Demirtaş, T.T., Irmak, G., and Gümüşderelioğlu, M. A bioprintable form of chitosan hydrogel for bone tissue engineering. Biofabrication **9,** 035003, 2017.

23. Hafezi, F., Shorter, S., Tabriz, A.G., *et al.* Bioprinting and preliminary testing of highly reproducible novel bioink for potential skin regeneration. Pharmaceutics **12,** 550, 2020.

24. Zhou, F., Hong, Y., Liang, R., *et al.* Rapid printing of bioinspired 3D tissue constructs for skin regeneration. Biomaterials **258,** 120287, 2020.

25. Heinrich, M.A., Liu, W., Jimenez, A., *et al.* 3D bioprinting: from benches to translational applications. Small **15,** e1805510, 2019.

26. Dempster, D.W., Compston, J.E., Drezner, M.K., *et al.* Standardized nomenclature, symbols, and units for bone histomorphometry: a 2012 update of the report of the ASBMR Histomorphometry Nomenclature Committee. J Bone Miner Res **28,** 2, 2013.

27. Mansfeldt, T., and Dohrmann, R. Chemical and mineralogical characterization of blast-furnace sludge from an abandoned landfill. Environ Sci Technol **38,** 5977, 2004.

28. Raafat, S.N., Amin, R.M., Elmazar, M.M., Khattab, M.M., and El-Khatib, A.S. The sole and combined effect of simvastatin and platelet rich fibrin as a filling material in induced bone defect in tibia of albino rats. Bone **117,** 60, 2018.

29. Firouzian, K.F., Zhang, T., Zhang, H., Song, Y., Su, X., and Lin, F. An image-guided intrascaffold cell assembly technique for accurate printing of heterogeneous tissue constructs. ACS Biomater Sci Eng **5,** 3499, 2019.

30. Rasperini, G., Pilipchuk, S.P., Flanagan, C.L., *et al.* 3D-printed bioresorbable scaffold for periodontal repair. J Dent Res **94(9 Suppl)),** 153S, 2015.

31. Lee, C.H., Hajibandeh, J., Suzuki, T., Fan, A., Shang, P., and Mao, J.J. Three-dimensional printed multiphase scaffolds for regeneration of periodontium complex. Tissue Eng Part A **20,** 1342, 2014.

32. Chen, J., Chen, H., Li, P., *et al.* Simultaneous regeneration of articular cartilage and subchondral bone *in vivo* using MSCs induced by a spatially controlled gene delivery system in bilayered integrated scaffolds. Biomaterials **32,** 4793, 2011.

33. Daly, A.C., Freeman, F.E., Gonzalez-Fernandez, T., Critchley, S.E., Nulty, J., and Kelly, D.J. 3D bioprinting for cartilage and osteochondral tissue engineering. Adv Healthc Mater **6,** 1700298, 2017.

34. Idaszek, J., Costantini, M., Karlsen, T.A., *et al.* 3D bioprinting of hydrogel constructs with cell and material gradients for the regeneration of full-thickness chondral defect using a microfluidic printing head. Biofabrication **11,** 044101, 2019.

35. Liu, P., Li, Q., Yang, Q., *et al.* Three-dimensional cell printing of gingival fibroblast/acellular dermal matrix/gelatin–sodium alginate scaffolds and their biocompatibility evaluation *in vitro*. RSC Adv **10,** 15926, 2020.

36. Sakai, S., Hirose, K., Taguchi, K., Ogushi, Y., and Kawakami, K. An injectable, *in situ* enzymatically gellable, gelatin derivative for drug delivery and tissue engineering. Biomaterials **30,** 3371, 2009.

37. Lim, K.S., Schon, B.S., Mekhileri, N.V., *et al.* New visible-light photoinitiating system for improved print fidelity in gelatin-based bioinks. ACS Biomater Sci Eng **2,** 1752, 2016.

38. Pan, T., Song, W., Cao, X., and Wang, Y. 3D bioplotting of gelatin/alginate scaffolds for tissue engineering: influence of crosslinking degree and pore architecture on physicochemical properties. J Mater Sci Technol **32,** 889, 2016.

39. Lee, A., Hudson, A.R., Shiwarski, D.J., *et al.* 3D bioprinting of collagen to rebuild components of the human heart. Science **365,** 482, 2019.

40. Zhang, L., Yang, G., Johnson, B.N., and Jia, X. Three-dimensional (3D) printed scaffold and material selection for bone repair. Acta Biomater **84,** 16, 2019.

41. Lee, K.Y., and Mooney, D.J. Alginate: properties and biomedical applications. Prog Polym Sci **37,** 106, 2012.

42. Axpe, E., and Oyen, M.L. Applications of alginate-based bioinks in 3D bioprinting. Int J Mol Sci **17,** 1976, 2016.

43. Ji, S., and Guvendiren, M. Recent advances in bioink design for 3D bioprinting of tissues and organs. Front Bioeng Biotechnol **5,** 23, 2017.

44. Wu, Z., Li, Q., Xie, S., Shan, X., and Cai, Z. *In vitro* and *in vivo* biocompatibility evaluation of a 3D bioprinted gelatin-sodium alginate/rat schwann-cell scaffold. Mater Sci Eng C Mater Biol Appl **109,** 110530, 2020.

45. Zhang, J., Wehrle, E., Adamek, P., *et al.* Optimization of mechanical stiffness and cell density of 3D bioprinted cell-laden scaffolds improves extracellular matrix mineralization and cellular organization for bone tissue engineering. Acta Biomater **114,** 307, 2020.

46. Wüst, S., Godla, M.E., Müller, R., and Hofmann, S. Tunable hydrogel composite with two-step processing in combination with innovative hardware upgrade for cell-based three-dimensional bioprinting. Acta Biomater **10,** 630, 2014.

47. Nair, K., Gandhi, M., Khalil, S., *et al.* Characterization of cell viability during bioprinting processes. Biotechnol J **4,** 1168, 2009.

48. Chang, R., Nam, J., and Sun, W. Effects of dispensing pressure and nozzle diameter on cell survival from solid freeform fabrication–based direct cell writing. Tissue Eng Part A **14,** 41, 2008.

49. Lin, H.-R., and Yeh, Y.-J. Porous alginate/hydroxyapatite composite scaffolds for bone tissue engineering: preparation, characterization, and *in vitro* studies. J Biomed Mater Res B Appl Biomater **71B,** 52, 2004.

50. Cai, X., ten Hoopen, S., Zhang, W., *et al.* Influence of highly porous electrospun PLGA/PCL/nHA fibrous scaffolds on the differentiation of tooth bud cells *in vitro*. J Biomed Mater Res A **105,** 2597, 2017.

51. Holmes, B., Zhu, W., Li, J., Lee, J.D., and Zhang, L.G. Development of novel three-dimensional printed scaffolds for osteochondral regeneration. Tissue Eng Part A **21,** 403, 2015.

52. Nakayama, K.H., Hou, L., and Huang, N.F. Role of extracellular matrix signaling cues in modulating cell fate commitment for cardiovascular tissue engineering. Adv Healthc Mater **3,** 628, 2014.

53. Sartori, M., Pagani, S., Ferrari, A., *et al.* A new bi-layered scaffold for osteochondral tissue regeneration: *in vitro* and *in vivo* preclinical investigations. Mater Sci Eng C Mater Biol Appl **70,** 101, 2017.

54. Murphy, M.B., Blashki, D., Buchanan, R.M., *et al.* Multi-composite bioactive osteogenic sponges featuring mesenchymal stem cells, platelet-rich plasma, nanoporous silicon enclosures, and peptide amphiphiles for rapid bone regeneration. J Funct Biomater **2,** 39, 2011.

55. Qu, D., Li, J., Li, Y., *et al.* Ectopic osteochondral formation of biomimetic porous PVA-n-HA/PA6 bilayered scaffold and BMSCs construct in rabbit. J Biomed Mater Res B Appl Biomater **96B,** 9, 2011.

56. Ogle, M.E., Segar, C.E., Sridhar, S., and Botchwey, E.A. Monocytes and macrophages in tissue repair: implications for immunoregenerative biomaterial design. Exp Biol Med **241,** 1084, 2016.

57. Londono, R., Dziki, J.L., Haljasmaa, E., Turner, N.J., Leifer, C.A., and Badylak, S.F. The effect of cell debris within biologic scaffolds upon the macrophage response. J Biomed Mater Res A **105,** 2109, 2017.

Address correspondence to:
Zhihui Tang, PhD
Second Clinical Division
Peking University School and Hospital of Stomatology
66 Anli Road
Beijing 100081
Chaoyang District
China

E-mail: zhihui_tang@bjmu.edu.cn

Hom-Lay Wang, PhD
Department of Periodontics and Oral Medicine
University of Michigan School of Dentistry
1011 North University Avenue
Ann Arbor, MI 48109-1078
USA

E-mail: homlay@umich.edu